coatings

MDPI

Article

CeO_2 Protective Material against CMAS Attack for Thermal–Environmental Barrier Coating Applications

Lei Guo [1,2,*], Yuanpeng Wang [1], Mingguang Liu [3], Yuan Gao [1] and Fuxing Ye [1,2,*]

[1] School of Materials Science and Engineering, Tianjin University, Tianjin 300072, China
[2] Tianjin Key Laboratory of Advanced Joining Technology, Tianjin University, Tianjin 300072, China
[3] Naval Logistics Academy, Tianjin 300450, China
* Correspondence: glei028@tju.edu.cn (L.G.); yefx@tju.edu.cn (F.Y.)

Abstract: Calcium–magnesium–alumina–silicate (CMAS) attack is a crucial issue for thermal–environmental barrier coatings (T/EBCs) with the ever-increasing operating temperature of turbine engines. In this study, CeO_2 has been demonstrated as a promising protective material for T/EBCs against CMAS attack. At 1300 °C, CeO_2 powder kept excellent phase and structural stability in molten CMAS; there were some CMAS constituents dissolved into the CeO_2 lattice to form a solid solution. With higher CeO_2 contents and longer duration time, more CeO_2 solid solution particles were formed, which acted as the nucleating agent for CMAS crystallization. As a result, apatite, anorthite and wollastonite crystalline products were easily generated. At 1300 °C for 10 h, CeO_2 pellets covered with CMAS powder had limited degradation, which was attributed to the rapid crystallization of molten CMAS due to the excellent nucleating agent effect of the precipitated CeO_2 solid solution.

Keywords: thermal–environmental barrier coating; calcium–magnesium–alumina–silicate (CMAS); CeO_2; crystallization; nucleating agent

Citation: Guo, L.; Wang, Y.; Liu, M.; Gao, Y.; Ye, F. CeO_2 Protective Material against CMAS Attack for Thermal–Environmental Barrier Coating Applications. *Coatings* **2023**, *13*, 1119. https://doi.org/10.3390/coatings13061119

Academic Editor: Cecilia Bartuli

Received: 7 May 2023
Revised: 3 June 2023
Accepted: 12 June 2023
Published: 18 June 2023

1. Introduction

Nickel-based superalloys suffer from extremely high temperatures due to the increasing inlet temperatures of turbine engines. Their operating temperatures generally do not exceed 1177 °C, and the temperature required for engine power and efficiency has exceeded the maximum tolerance range of nickel-based superalloys [1–5]. Ceramic matrix composites (CMCs) have recently received significant attention because they can maintain high strength at temperatures up to 1250 °C, which is about 150 °C higher than nickel-based superalloys and have a lower density (one-third of that of Ni alloys) [6,7]. Thus, they can be used as an alternative material for nickel-based superalloys. However, CMC materials also have some shortcomings, and the most notable is the water vapor oxidation, which causes their severe recession and component failure. Therefore, it is necessary to use environmental barrier coatings (EBCs) that can block water and oxygen for improved corrosion resistance, thereby prolonging the service life of engine hot-section components. In recent years, a thermal–environmental barrier coating (T/EBC) has been an emerging system of EBCs that protects some lightweight and high-temperature SiC/SiC CMC components [3,6,8].

The concept of a T/EBC system was first proposed by NASA. It is actually a double-layer structure, the top layer being composed of a thermal barrier coating (TBC) material, the second layer being an EBC material, and there is a composition gradient layer between the TBC and EBC [9]. In this coating system, the top layer is ZrO_2 (mostly yttria-stabilized zirconia, YSZ) or HfO_2-based TBCs, while rare earth silicates and rare earth aluminates are used as multicomponent EBCs [10,11]. This multi-component, multi-layer coating system has low thermal conductivity, and forms no obvious cracks after 300 h gradient thermal cycling at temperatures up to 1650 °C, showing good cycle durability and resistance to

water and oxygen corrosion [12]. The T/EBC system requires a proper coefficient of thermal expansion (CTE) to match the CMC matrix to ensure excellent properties such as high-temperature performance, chemical compatibility, mechanical strength (high hardness and toughness) against fracture, erosion, and impact damage [13]. Ytterbium silicate has become the most promising EBC due to its excellent high-temperature stability, good thermal shock resistance, and good coefficient of thermal expansion matching with SiC/SiC CMCs.

In addition to the performance required above, T/EBC also needs excellent resistance to high-temperature corrosion. During aero-engine operation, siliceous debris (such as sand, dust, and volcanic ash, mainly consisting of CaO, MgO, Al_2O_3, SiO_2, CMAS) is ingested by the intake air and deposited on the surface of components, which corrodes T/EBCs, significantly decreasing their high-temperature capability [14–17]. For practical applications, T/EBCs inevitably face CMAS issues. Therefore, it is necessary to actively explore methods to prevent CMAS attack to T/EBCs [18–20].

CMAS penetration into T/EBCs causes a reaction between them, which largely destroys the coating microstructure and reduces the strain tolerance of the coating. Hence, suppressing the melt penetration is the key to alleviating CMAS attack to T/EBCs, and some strategies have been proposed. One is designing a coating composition which can promote melt crystallization when it comes into contact with the molten CMAS, and the other is to apply a protective layer on the coating surface to inhibit penetration [21]. Poerschke et al. prepared T/EBCs of ytterbium silicate/hafnate and found that they could promote CMAS crystallization and prevent melt infiltration [22]. Godbole et al. studied the apatite and garnet stability in the Al–Ca–Mg–Si–(Gd/Y/Yb)–O system [23]. The results showed that rare earth plays an important role in the formation of apatite and garnet crystalline phases, but no matter which crystalline phase is formed, they all have positive functions for T/EBC materials to prevent CMAS melt infiltration. However, due to the extremely high temperatures of the coating surface, the CMAS attack is severe. Thus, applying a protective layer on the T/EBC surface might be more useful [24].

Since the structure of T/EBCs takes the TBC as the top layer, the preparation method for the TBC protective layer can be referred to when preparing the protective layer. Common protective layers are made of Pd–Ag, Pt, Pd, etc., which are inert to react with CMAS, thereby preventing the melt penetration [25]. However, this method is highly limited in practice because of its high cost. Reports have shown that coatings containing large amounts of rare earth elements are highly resistant to CMAS penetration due to the rapid promotion of melt crystallization, and based on this, some researchers have proposed that applying a protective layer made of rare earth oxides on coating surfaces might be effective in inhibiting CMAS penetration [26–28].

Among all rare earth oxides, CeO_2 is very special, with a valence of +4 rather than +3 for other rare earth elements. In this work, the interaction behavior of CMAS and CeO_2 powders was first investigated to evaluate the high-temperature stability of CeO_2 in the presence of molten CMAS, identifying the possible reaction products and their evolution laws with the CeO_2 content and duration time. Then, CMAS powder was covered on CeO_2 pellets and heat treated at 1300 °C, and the results revealed that the pellets were hardly damaged by CMAS and there was no melt penetration. This study explores the feasibility of CeO_2 as a protective layer material for T/EBCs against CMAS attack.

2. Experimental Procedure

2.1. Materials

A laboratory-simulated CMAS was prepared according to our previous study and other researchers [29,30] with a chemical composition of $33CaO–9MgO–13AlO_{1.5}–45SiO_2$ (mol%). Figure 1 shows the preparation process of the CMAS powder. Four raw materials with a particle size of 500 μm (CaO, MgO, Al_2O_3, and SiO_2; Jiangtian Chemical Technology Ltd., Tianjin, China) were weighed at the appropriate molar ratio, suspended in a certain amount of deionized water, and then planetary ball milling was carried out at a speed of 400 rpm for 10 h (QM-3SP4, Nanjing University Instrument Factory, Nanjing, China).

The resultant slurry was put into an oven and dried at 120 °C for 10 h, followed by heat treatment at 1550 °C at a rate of 10 °C/min and maintained in a box furnace (SX-1600 °C, Zhonghuan Electric Furnace Ltd., Tianjin, China) for 1 h. Finally, the molten CMAS was poured into a copper plate in water to obtain CMAS glass. The prepared CMAS block was hammered into small pellets with a volume of 0.4 to 0.7 cm^3, ground into powder, and passed through a 200 mesh sieve. The melting point of this CMAS was measured by our previous experiments, with the value of about 1230~1240 °C [31].

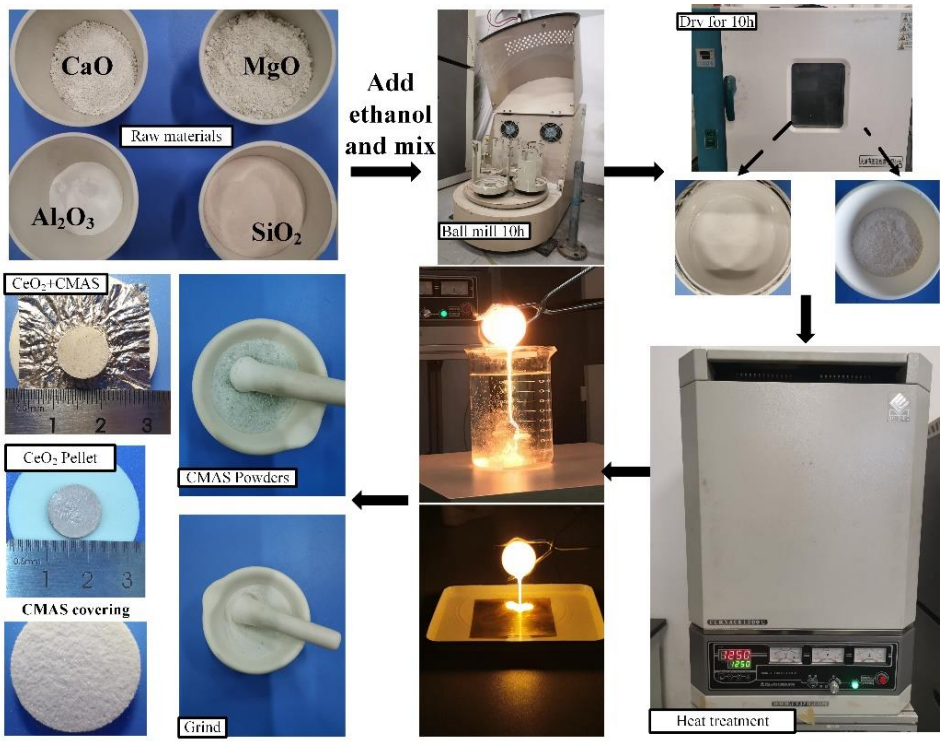

Figure 1. The process of CMAS preparation and its covering on CeO_2 pellets.

About 0.5 g of the prepared CMAS powder was mixed with CeO_2 of 5×10^{-4} mol and 1×10^{-3} mol in two portions, and the mixed powders were pressed into cylindrical pellets with a diameter of 10 mm. The purpose of two portions is to study the effect of CeO_2 concentration on the interaction behavior with CMAS. The pellet was placed in the center of a 30 mm × 30 mm platinum crucible and then placed on the corundum sheet (Figure 1). A box furnace (SX-1300 °C, Zhonghuan Electric Furnace Ltd., Tianjin, China) was used, and the heat treatment conditions were 1300 °C for 2 h and 10 h. The temperature of 1300 °C is related to the application of T/EBCs. After the dwelling time, the samples were taken out for air cooling to preserve the state of the CMAS and CeO_2 at high temperatures. Note that the temperature of 1300 °C and air cooling adopted here are to avoid CMAS self-crystallization for distinguishing whether CeO_2 can cause CMAS crystallization.

As depicted in Figure 1, 1.5 g CeO_2 was also weighed and pressed into a cylindrical pellet with a diameter of 15 mm. CMAS powders were uniformly covered on the surface of the pellet and kept at 1300 °C for 10 h. Then, the samples were cooled to room temperature in the furnace. The purpose of the slow cooling in the furnace is to prolong the molten state of CMAS. If CMAS cannot penetrate and corrode the CeO_2 pellet after 10 h dwelling time and slow cooling in the furnace, it can be demonstrated that CeO_2 has a significant effect on preventing CMAS penetration and corrosion.

2.2. Characterizations

The differential scanning calorimetry (DSC; STA 449 C, NETZSCH (Shanghai) Ltd., Shanghai, China) analysis of CMAS (0.5 g) and CeO_2 (5×10^{-4} mol) powders was performed from room temperature to 1300 °C at a heating rate of 10 °C/min, and the purpose

of DSC was to see whether a reaction between CeO_2 and CMAS occurs. After the heat treatment, the mixed powders of CMAS and CeO_2 were characterized by X-ray diffractometer (XRD; D8 Advanced, Bruker, Karlsruhe, Germany) with CuKα radiation to confirm the inference and characterize the phase composition. The cross-sectional images, EDS mapping, and element composition were characterized by a scanning electron microscope (SEM; Nova Nanosem 430, FEI, Hillsboro, OR, USA) equipped with an energy dispersive spectroscopy (EDS; Genesis XM2, EDAX, Warrendale, PA, USA).

3. Results and Discussions

3.1. Interaction Behavior of CeO_2 and CMAS Powders

Figure 2 shows the morphology of the CeO_2 and CMAS powder mixture after heat treatment at 1300 °C for 2 h and 10 h. The resultant samples all exhibit an opaque appearance. By comparing Figure 2a,b, it can be found that increasing the CeO_2 content in the mixture from 5×10^{-4} mol to 1×10^{-3} mol leads to a decrease in the spreading area from 3.8 cm^2 to 2.14 cm^2. In Figure 2c,d, the spreading areas of the samples with 5×10^{-4} mol and 1×10^{-3} mol CeO_2 are 1.96 cm^2 and 1.2 cm^2, respectively. This indicates that the spreading area of CeO_2 + CMAS mixture decreases with the increase of the CeO_2 content and the duration time. It is known that the spreading area of melt is related to its viscosity, i.e., a smaller spreading area means higher melt viscosity. Hence, one could conclude that increasing the CeO_2 content and the duration can increase the viscosity of the molten mixture, and the detailed discussion on the viscosity will be given in the following section.

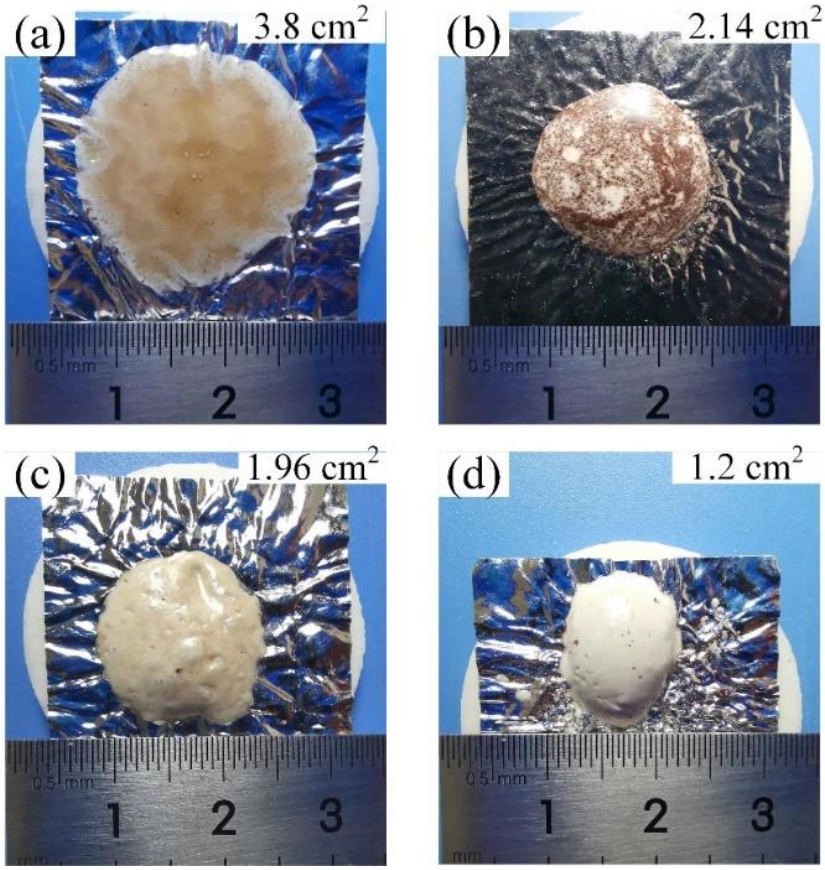

Figure 2. Morphology of the mixture of 0.5 g CMAS and different amounts of CeO_2 after heat treatment at 1300 °C for 2 h (**a**,**b**) and 10 h (**c**,**d**). (**a**) 5×10^{-4} mol CeO_2, (**b**) 1×10^{-3} mol CeO_2, (**c**) 5×10^{-4} mol CeO_2, (**d**) 1×10^{-3} mol CeO_2.

Figure 3 shows the XRD patterns of the CeO_2 + CMAS mixture after heat treatment at 1300 °C. The phase mainly consists of CeO_2 solid solution. In addition, some diffraction

peaks ascribed to anorthite ($CaAl_2Si_2O_8$) and pseudo-wollastonite ($CaSiO_3$) phases are detected [32]. CeO_2 belongs to a face-centered cubic structure, in which Ce^{4+} is densely packed according to the face-centered cubic structure and O^{2-} occupies all the tetrahedral voids [33,34]. Thus, the formation of CeO_2 solid solution results from the substitution of Ce^{4+} by the CMAS constituents, such as Ca^{2+}, Al^{3+}, and Si^{4+}, which will be demonstrated by the following SEM observations.

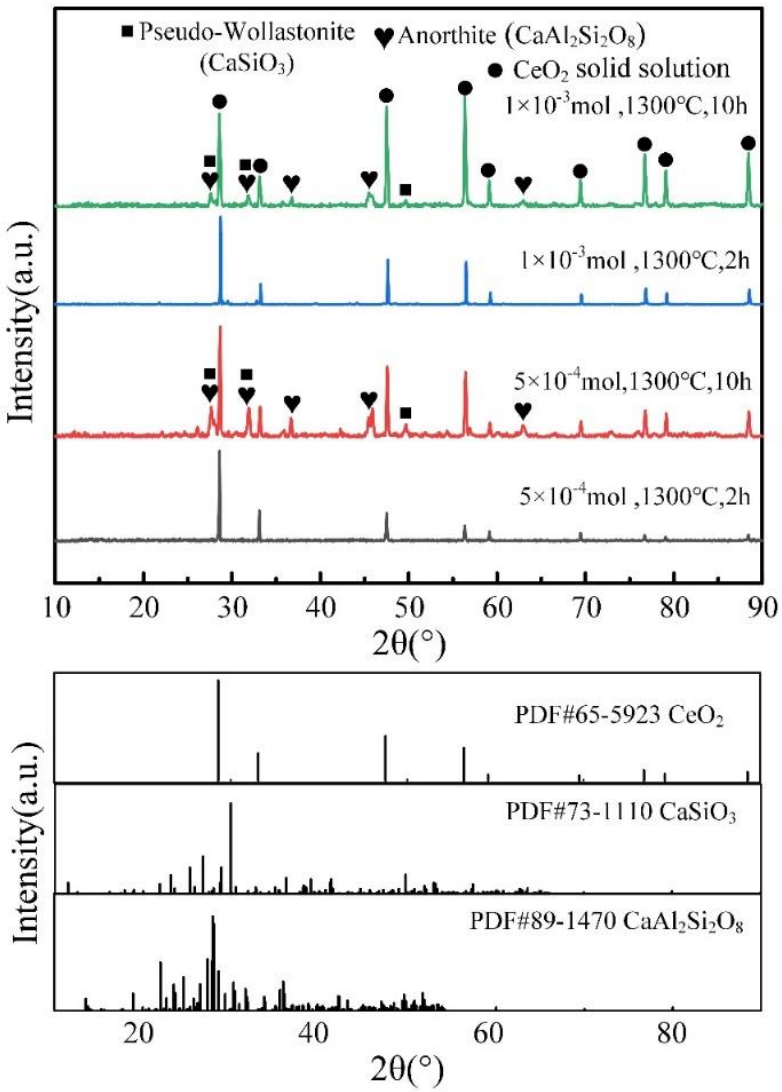

Figure 3. XRD patterns of CMAS + CeO_2 mixture after heat treatment at 1300 °C.

Figure 4 is the DSC curve of the CMAS + CeO_2 mixture. It is reported that CMAS does not have a specific melting point but has a certain temperature range of 1230~1250 °C [27]. In this experiment, two exothermic peaks can be found at ~1040 and 1210 °C, which may be due to the self-crystallization of CMAS leading to the formation of anorthite and wollastonite phases [31]. The melting point of CMAS used in this experiment is about 1230~1240 °C, and the absence of an endothermic peak at this temperature range may be attributed to the thermal overlap of melting and crystallization. Therefore, the endothermic peak at ~1260 °C may be formed by the thermal overlap involving crystallization and melting in the CMAS + CeO_2 mixture [35]. It should be noted that the formation of self-crystallizing products does not mean that the self-crystallization behavior is dominant, but just implies that it can occur in a specific temperature region.

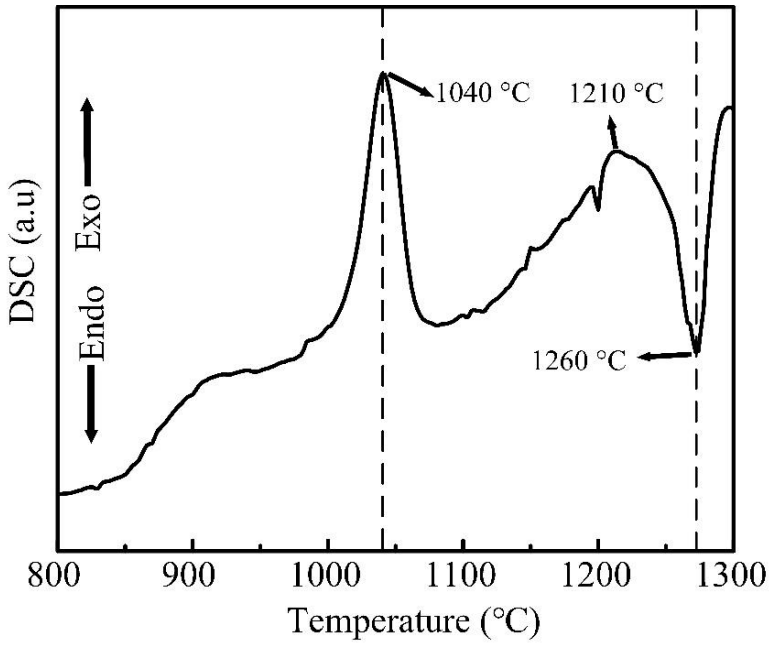

Figure 4. DSC curve of the mixture of CMAS + 5 × 10^{-4} mol CeO_2.

Figure 5a shows the cross-sectional microstructure of the mixture of CMAS + 5 × 10^{-4} mol CeO_2 after heat treatment at 1300 °C for 2 h and the corresponding EDS results. There are many white globular particles, and the EDS mapping results demonstrate that they are composed of Ce and O elements. Previous studies [31,36–39] have shown that the crystalline products formed by the reaction or CMAS self-crystallization are generally rod-shaped (e.g., apatite), so this white globular phase is likely to be CeO_2 solid solution due to reprecipitation, which is different from the original CeO_2 particles, which have a strip-like appearance, as shown in Figure 5b. The remaining places where Ca, Al, and Si are gathered are the residual CMAS melt. Figure 5c is a magnification of the red rectangle in Figure 5a, and the composition positions 1 and 2 are measured. The globular phase CeO_2 solid solution (position 1) can be found to contain Ca, Si, and Al. The Si content reach 18.59%, and those of Ca and Al are equivalent, which is about one-third of that of the Ce element. The large amount of Si in the globular products is attributed to the fact that Si^{4+} has a smaller size than Ca^{2+}, Mg^{2+}, and Al^{3+}, and its valence is the same as Ce^{4+}. Apart from these globular crystals being formed due to the dissolution and reprecipitation mechanism, no other phases could be observed, suggesting a limited reaction between CMAS and CeO_2 particles under this condition.

When the CeO_2 content in the mixture increases to 1 × 10^{-3} mol, some rod-like crystals are formed, as shown in Figure 6a. EDS analysis of regions 1, 2, and 3 suggests that the chemical compositions of these crystals are close to that of the apatite phase. Combined with their morphologies, these rod-like crystals could be determined as Ce-apatite. Figure 6b is an enlarged image of the region with a large number of globular crystals, which is similar to those observed in Figure 5, and could be confirmed as CeO_2 solid solution.

Figure 5a reveals that the mixture of CMAS + 5 × 10^{-4} mol CeO_2 can only form globular crystals of CeO_2 solid solution at 1300 °C for 2 h. Here, we prolonged the duration time, and find dark contrasted and white contrasted rod-like crystals in the cross-sectional images, as shown in Figure 7. EDS mapping analysis indicates that the dark contrasted crystals are mainly composed of Ca, Si, and Al elements, which could be confirmed as the anorthite phase. The white contrasted globular crystals are rich in Ce, together with some Si, Al, and Ca, indicative of the formation of CeO_2 solid solution. The rod-like crystals in the region highlighted by a yellow rectangular box in Figure 7b are apatite. The presence of apatite and anorthite phases indicates that prolonging the duration time could promote the reaction between CeO_2 and CMAS, but the formation ability of apatite is much lower than that of CeO_2 solid solution.

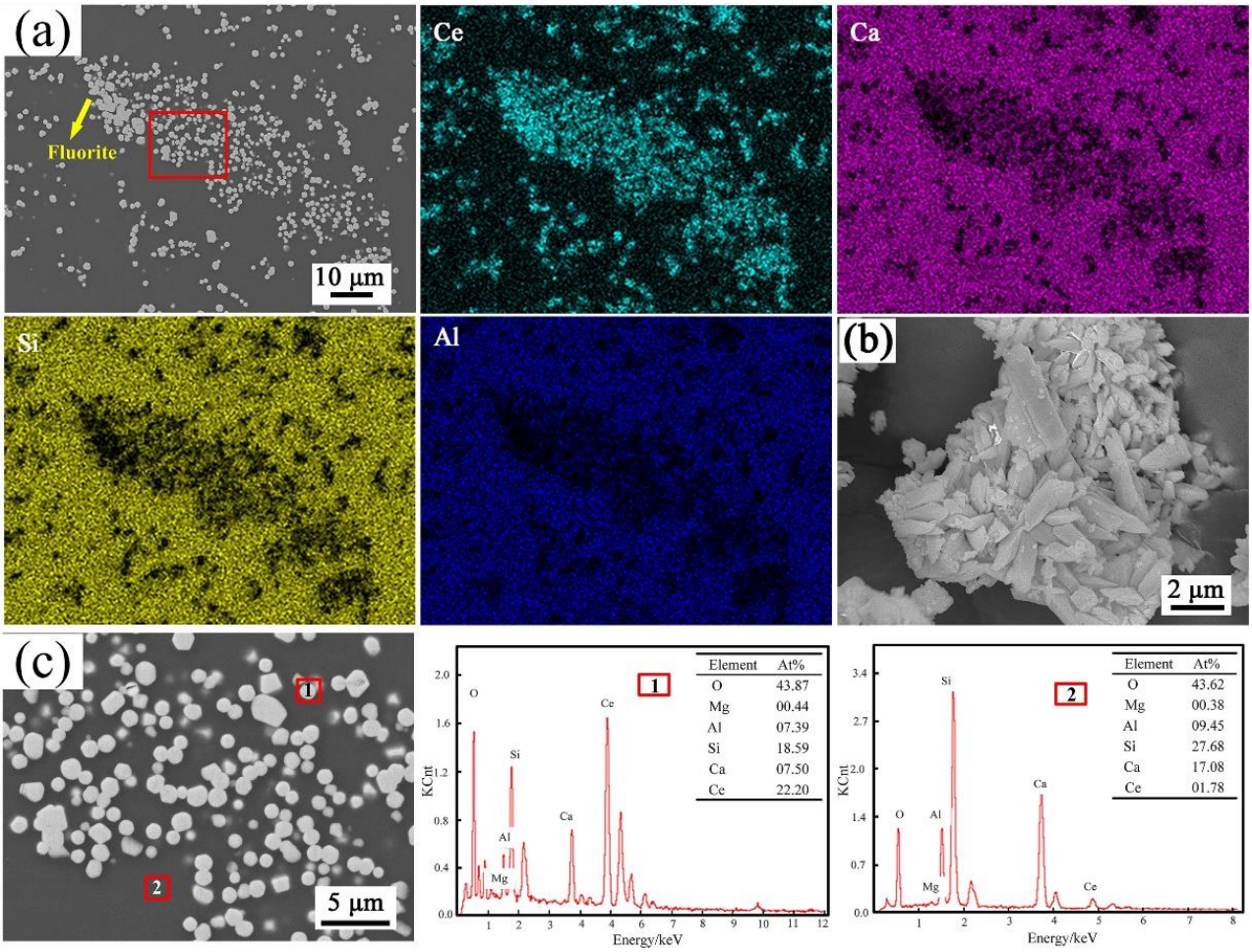

Figure 5. Cross-sectional microstructure of the mixture of CMAS + 5 × 10^{-4} mol CeO_2 after heat treatment at 1300 °C for 2 h (**a**), and the original morphology of CeO_2 powder (**b**). The enlarged image of the region highlighted by a red rectangle in (**a**) is shown in (**c**). Corresponding EDS mapping results of Ce, Ca, Si, and Al, and elemental compositions of the marked areas (**1**,**2**) in (**c**) are also presented.

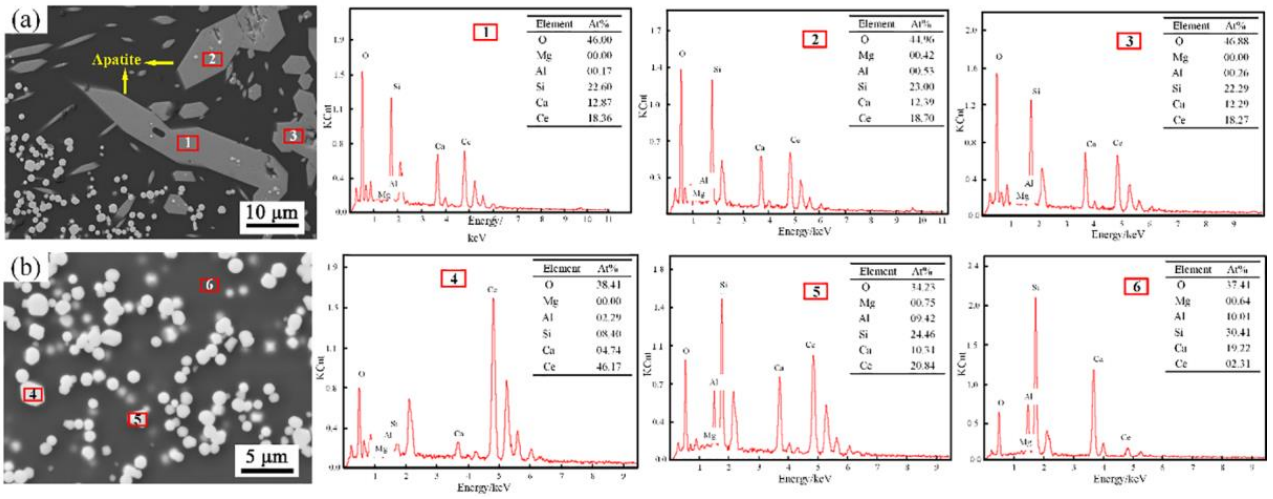

Figure 6. Cross-sectional microstructure of the mixture of CMAS + 1 × 10^{-3} mol CeO_2 after heat treatment at 1300 °C for 2 h (**a**) and its enlarged view (**b**). EDS results of the marked areas (**1**–**3**) in (**a**) and (**4**–**6**) in (**b**) are also presented.

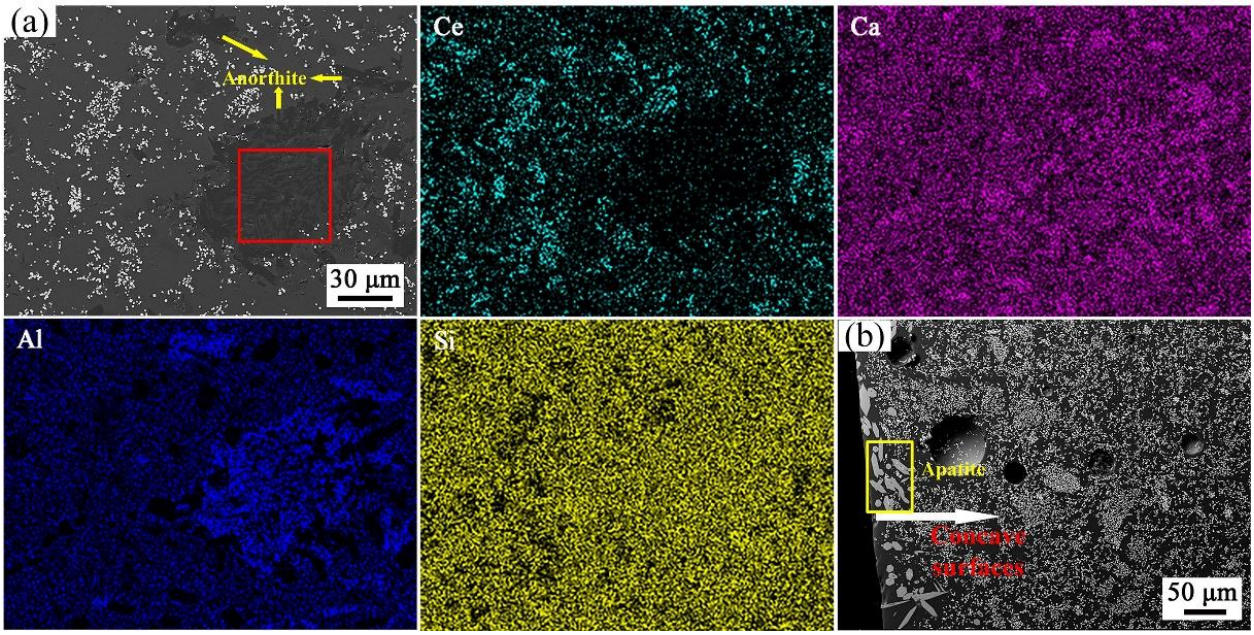

Figure 7. Cross-sectional microstructure of the mixture with CMAS + 5 × 10^{-4} mol CeO_2 after heat treatment at 1300 °C for 10 h (**a**,**b**). Corresponding EDS mapping of Ce, Ca, Al, Si, O, and elemental composition of marked areas are presented.

Figure 8 shows the cross-sectional SEM images of CMAS + 1 × 10^{-3} mol CeO_2 after heat treatment at 1300 °C for 10 h. More globular crystals of CeO_2 solid solution are formed, and the apatite crystals grow to more than 50 μm in length. In Figure 8b, an obvious anorthite phase can be found, and the region highlighted by a red rectangular box is enlarged in Figure 8c. The chemical compositions analysis indicates that crystals 1 and 3 are CeO_2 solid solution and anorthite, respectively. In residual CMAS (region 2), very limited Ce could be detected.

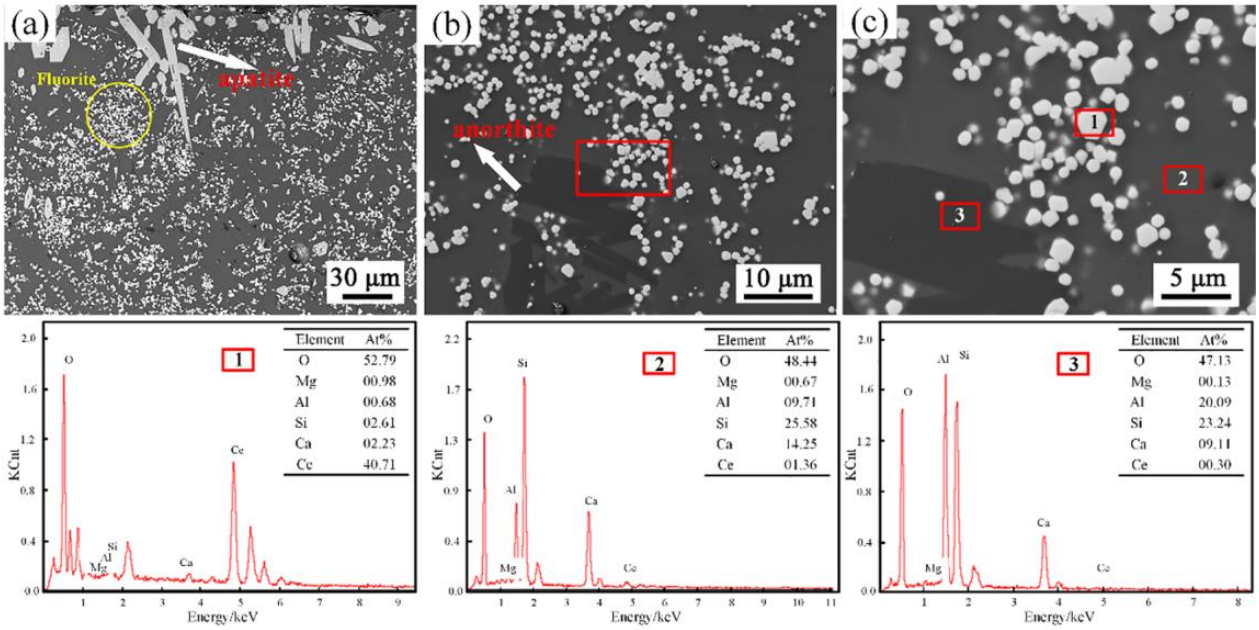

Figure 8. Cross-sectional microstructure of the mixture with CMAS + 1 × 10^{-3} mol CeO_2 after heat treatment at 1300 °C for 10 h (**a**–**c**), where (**c**) is an enlarged view of (**b**). EDS results of marked regions (**1**–**3**) in (**c**) are also presented.

3.2. Effects of the CeO_2 Content and Duration Time on the Crystalline Products Formation

Based on the aforementioned observations, it can be found that some CeO_2 prefers to dissolve in molten CMAS and then reprecipitate to form CeO_2 solid solution, gathering some amounts of Si, Ca, and Al, among which the Si content is the highest. The reaction between CeO_2 and CMAS is not vigorous, indicating that CeO_2 can maintain phase and structural stability in the presence of CMAS. However, increasing the CeO_2 content and duration time can promote the reaction, which leads to the formation of apatite and CMAS self-crystallization products such as anorthite and wollastonite phases.

According to our previous research, CMAS self-crystallization does not occur at fast cooling rates such as air cooling [31]. However, CMAS self-crystallization products were detected by XRD and SEM in this study. This may be because the formed CeO_2 solid solution particles act as a nucleating agent for anorthite and wollastonite phases [40]. Additionally, the formation of anorthite is also affected by the Al content in the melt, and increasing the Al content can promote to produce anorthite [41–43]. As mentioned above, the content of Si in CeO_2 solid solution is higher than that of Al; in other words, the formation of CeO_2 solid solution consumes more Si, and the Al content in the CMAS is increased. As a result, the self-crystallization product of anorthite is produced. In the SEM observations, wollastonite was not found, possibly because the contrast of wollastonite is similar to that of the residual CMAS and its amount is low (its XRD peaks intensities are very low). In addition, self-crystallization products cannot be detected by XRD until the duration time is prolonged to 10 h. This indicates that CMAS self-crystallization needs time. The longer the duration of mixing CeO_2 and CMAS, the more obvious the effect of CeO_2 as the nucleating agent, and the more CMAS self-crystallization products produced.

In Figure 3, no apparent apatite peaks appear in the XRD patterns when the CeO_2 content and duration time increase. The main reason may be related to the detection position. In this experiment, the sample is hemispherical (Figure 2), with a flat circular bottom and a concave top surface. According to the non-uniform nucleation principle, the concave surface has the highest nucleation efficiency because the smaller volume of crystal embryo can reach the critical nucleation radius. Meanwhile, nucleation also depends on defects such as interface impurities in the system, which can significantly reduce the free energy required for nucleation, so crystallization often starts from these interfaces (Figure 7b). Therefore, in the reaction between CeO_2 and CMAS, apatite nucleates mainly near the concave surface and grows oriented along the maximum temperature gradient (perpendicular to the surface) [44]. However, this study selected the circular plane at the bottom for XRD measurements, which leads to the absence of apatite characteristic peaks in XRD patterns.

Increasing the CeO_2 content and duration time can both promote the formation of the apatite phase, and increasing the duration time is more effective. At a lower CeO_2 content, the main product is CeO_2 solid solution, and the residual CMAS melt does not have enough Ce to produce apatite. Thus, increasing the CeO_2 content can increase the Ce amount in the molten CMAS, which is beneficial to trigger apatite formation. Additionally, under the prolonged duration time, the action time of the nucleating agent of CeO_2 solid solution particles is longer, and more Ce could be dissolved in the molten CMAS to promote the formation of the apatite phase. It has been reported that the dissolution–reprecipitation of particles in molten CMAS is a dynamic process [45,46]; thus, in this study, the Ce distribution in the melt is also dynamic. As mentioned above, in the case of a short duration time, the precipitated CeO_2 solid solution particles take away a large amount of Ce. During the prolonged heat treatment, compositional fluctuations occur in the molten CMAS, which favors the nucleation and growth of the apatite phase. As a result, non-uniformly nucleated apatite is found at concave surfaces.

After clarifying the interaction behavior and product formation mechanisms, the spreading areas and viscosity changes of the molten mixture of CMAS +CeO_2 could be explained (Figure 2). In silicate melts, the viscosity is determined mainly by Ca/Si, and the higher the Ca/Si, the lower the viscosity (inversely proportional) [47,48]. During the

interaction of CeO_2 and CMAS, with the increase of the CeO_2 content and the duration time, more apatite is produced, which consumes a large amount of Ca in the CMAS melt. As a result, the Ca/Si ratio decreases, causing an increase in the melt viscosity. Therefore, the spreading areas of the molten mixture of CMAS + CeO_2 decrease with the increase of the CeO_2 content and duration time. Note that enhancing the viscosity could drag the melt penetration in the coatings, which is beneficial for alleviating CMAS attack to TBCs.

3.3. Interface Interaction between Molten CMAS and CeO_2 Pellets

To evaluate whether CeO_2 can be used as a protective layer material against CMAS attack, CeO_2 pellets were used and covered with CMAS powder followed by heat treatment. This case could be approximately considered as the mixture of 1×10^{-3} mol CeO_2 with CMAS in the above sections. Figure 9 is a cross-sectional view of the CeO_2 pellet. It can be found that it is compact and free of microcracks but has some pores. A portion of Figure 9a is enlarged and shown in Figure 9b; some pores are found in the pellet. Since TBCs are usually designed to have some pores for stress tolerance, the pellets used for CMAS corrosion experiments need pores for more accurate simulation.

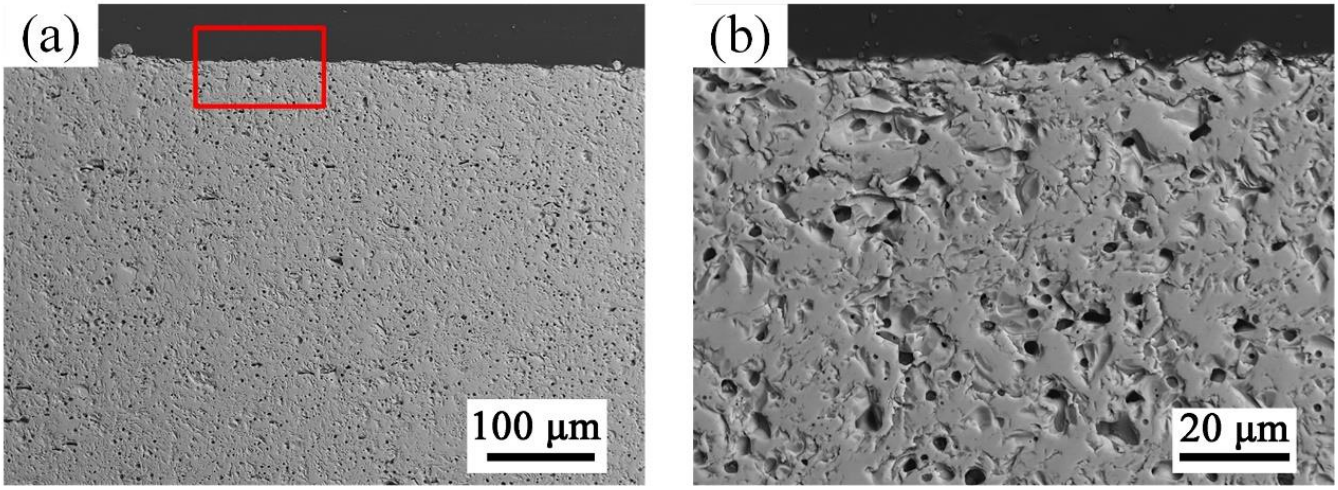

Figure 9. Cross-sectional morphology of CeO_2 pellet (**a**). The enlarged image of the region highlighted by a red rectangle in (**a**) is shown in (**b**).

The cross-sectional view of the CeO_2 pellet with CMAS after heat treatment at 1300 °C for 10 h and the corresponding EDS results are shown in Figure 10. It can be observed that the pellet microstructure has almost no change, and very limited CMAS constituent elements are detected in the pellet. On the pellet surface, a thick layer consisting of many white contrasted particles, dark contrasted strip-like crystals, and slight dark contrasted compounds can be found. According to the EDS mapping analysis, the white contrasted particles are rich in Ce and have some other elements, which could be confirmed as the CeO_2 solid solution phase. The dark contrasted strip-like crystals are mainly composed of Ca and Al, which could be identified as the anorthite phase. The region highlighted by a blue rectangle box in Figure 10a was magnified and shown in Figure 10b. It is clear that no CMAS penetration could be found in the pellet, and its microstructure is not destroyed. The EDS result of the pellet (region 1) indicates that the pellet is almost pure CeO_2. Region 2 is composed of Ca, Si, and O, and based on their chemical composition ratio, the compound could be determined to be $CaSiO_3$ wollastonite phase. The EDS result of region 3 further confirms that the dark contrasted strip-like crystals are $Ca_2Al_2Si_2O_8$ anorthite.

The limited penetration ability of molten CMAS in the CeO_2 pellet could be attributed to the rapid crystallization of the melt. At high temperatures, the interaction of molten CMAS and the CeO_2 pellet at their interface causes some amount of Ce dissolution into the melt, which quickly migrates into the entire molten CMAS on the pellet surface. As mentioned above, some CeO_2 solid solution particles are precipitated, which can be used

as the nucleating agent for CMAS crystallization. As a result, anorthite and wollastonite phases are formed, largely increasing the viscosity of the melt. As shown in Figure 10, no CMAS glass remains after the heat treatment, and all has been crystallized, indicating that CeO_2 solid solution particles have an effective function on promoting CMAS crystallization when used as the nucleating agent. Additionally, the absence of apatite phase in the crystalline layer further implies that CeO_2 has a high stability in molten CMAS, which causes insufficient Ce to be dissolved in the melt to trigger the formation of the apatite phase.

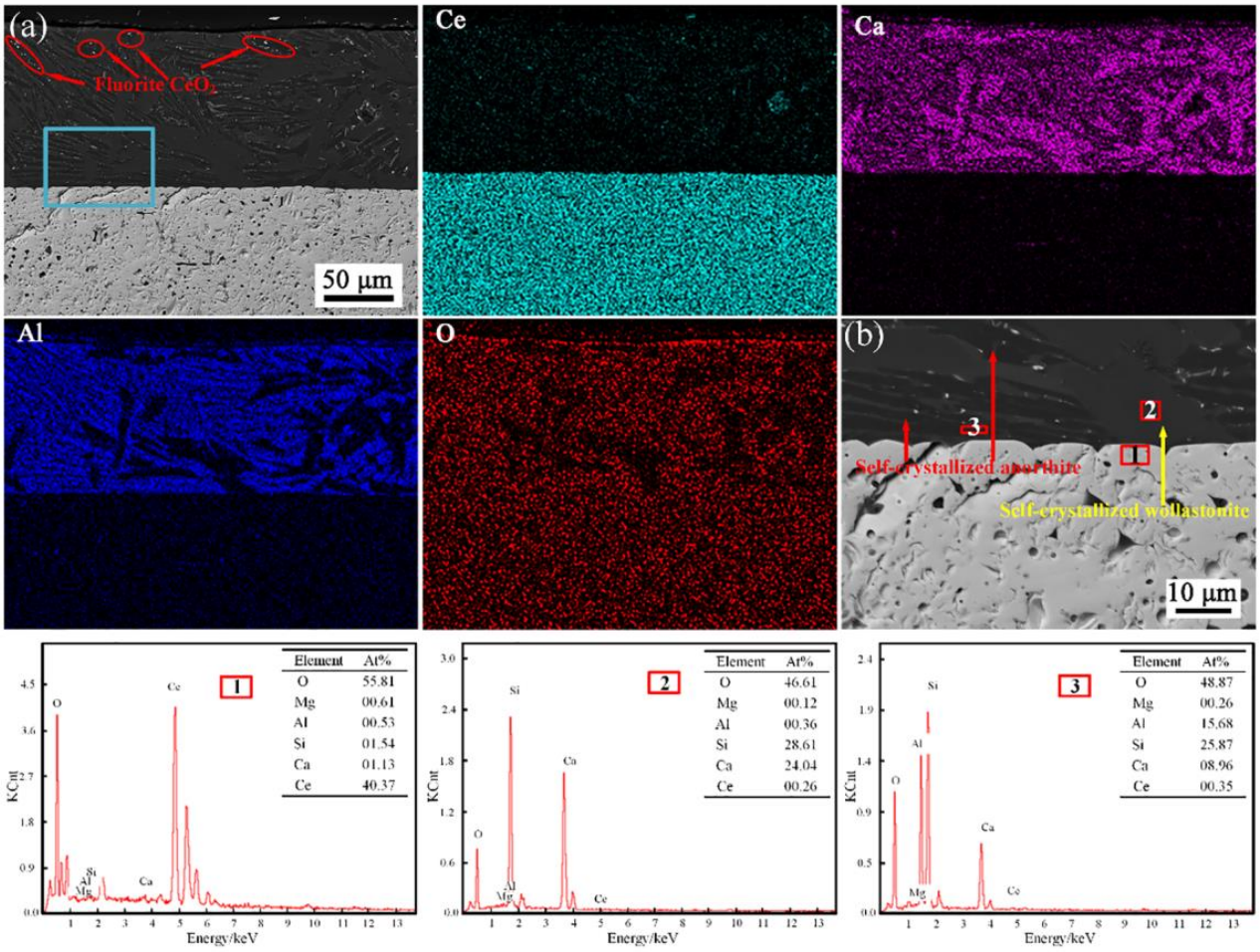

Figure 10. Cross-sectional microstructures of CeO_2 pellet subjected to CMAS at 1300 °C for 10 h (**a**). The enlarged image of the region highlighted by a blue rectangle in (**a**) is shown in (**b**). Corresponding EDS mapping of Ce, Ca, Si, and O, and elemental composition of the marked regions (**1**–**3**) in (**b**) are also presented.

Based on the investigation on the interaction behavior of CMAS and CeO_2, it could be found that CeO_2 is a useful material for mitigating CMAS attack to TBCs. Due to the excellent nucleating agent effect of the CeO_2 solid solution, one could design a T/EBC composition doped with Ce aiming to promote CMAS crystallization and suppress the melt penetration [49]. Meanwhile, based on the theory of optical basicity (OB), CeO_2 has a relatively moderate optical basicity (Λ = 1.01) compared to traditional TBC materials, which ensures that CeO_2 reacts with molten CMAS to form CeO_2 solid solution particles, promoting CMAS self-crystallization. Once the molten CMAS is crystallized, it is less harmful, and CeO_2 can maintain high stability [50,51]. Based on the high stability of CeO_2 in the presence of molten CMAS, a dense CeO_2 layer could be designed on the T/EBC surface, which might have an excellent function in inhibiting CMAS infiltration.

4. Conclusions

This study investigates the interaction behavior of CeO_2 powder/pellet and molten CMAS and discusses the effects of the CeO_2 content and duration time on the crystalline products. The following conclusions can be drawn:

(1) In the presence of molten CMAS, CeO_2 dissolves in the melt followed by precipitating many CeO_2 solid solution particles, in which Si, Ca, and Al are present and the Si content is the highest.

(2) The reaction between CMAS and CeO_2 is not vigorous at 1300 °C; only when the CeO_2 content is increased or the duration time prolonged to 10 h, a reaction product of apatite and some self-crystallization products of anorthite and wollastonite phases can be formed. During this reaction process, the CeO_2 solid solution particles are acted as the nucleating agent.

(3) After heat treatment at 1300 °C for 10 h, the CMAS on the CeO_2 pellet is completely crystallized due to Ce migration to the melt providing the nucleating agent. No CMAS penetration and no reaction products are found, indicating that CMAS crystallization is rapid and the Ce diffusion in the melt is limited, meaning excellent stability of CeO_2 in molten CMAS.

(4) CeO_2 can be used as a dopant in T/EBC to promote CMAS crystallization, and it is also a promising protective layer material on the T/EBC surface to inhibit CMAS penetration.

Author Contributions: Conceptualization, L.G.; methodology, L.G., Y.G. and Y.W.; software, L.G. and F.Y.; validation, L.G.; formal analysis, L.G., Y.W. and Y.G.; investigation, M.L. and Y.W.; resources, L.G. and Y.W.; data curation, Y.W. and Y.G.; writing—original draft preparation, Y.W. and Y.G.; writing—review and editing, M.L. and L.G.; supervision, L.G. and F.Y.; project administration, L.G.; funding acquisition, L.G. All authors have read and agreed to the published version of the manuscript.

Funding: This research is sponsored by the National Natural Science Foundation of China (Grants No. 51971156 and 52272070).

Institutional Review Board Statement: Not applicable.

Informed Consent Statement: Not applicable.

Data Availability Statement: Data presented in this article are available upon request from the corresponding author.

Conflicts of Interest: The authors declare no conflict of interest.

References

1. Hong, J.; Li, T.; Zheng, H.; Ma, Y. Applications of structural efficiency assessment method on structural-mechanical characteristics integrated design in aero-engines. *Chin. J. Aeronaut.* **2020**, *33*, 1260–1271. [CrossRef]
2. Zhang, B.; Song, W.; Wei, L.; Xiu, Y.; Xu, H.; Dingwell, D.B.; Guo, H. Novel thermal barrier coatings repel and resist molten silicate deposits. *Scr. Mater.* **2019**, *163*, 71–76. [CrossRef]
3. Chen, H.F.; Zhang, C.; Liu, Y.C.; Song, P.; Li, W.X.; Yang, G.; Liu, B. Recent progress in thermal/environmental barrier coatings and their corrosion resistance. *Rare Met.* **2019**, *39*, 498–512. [CrossRef]
4. Darolia, R. Thermal barrier coatings technology: Critical review, progress update, remaining challenges and prospects. *Int. Mater. Rev.* **2013**, *58*, 315–348. [CrossRef]
5. Bakan, E.; Vaßen, R. Ceramic top coats of plasma-sprayed thermal barrier coatings: Materials, processes, and properties. *J. Therm. Spray Technol.* **2017**, *26*, 992–1010. [CrossRef]
6. Diaz, O.G.; Axinte, D.; Butler-Smith, P.; Novovic, D. On understanding the microstructure of SiC/SiC Ceramic Matrix Composites (CMCs) after a material removal process. *Mater. Sci. Eng. A* **2018**, *743*, 1–11. [CrossRef]
7. Dicarlo, J.A. Advances in SiC/SiC composites for aero-propulsion. *M. Ceram. Matrix Compos.* **2014**, 217–235. [CrossRef]
8. Fang, G.; Gao, X.; Song, Y. A Review on Ceramic Matrix Composites and Environmental Barrier Coatings for Aero-Engine: Material Development and Failure Analysis. *Coatings* **2023**, *13*, 357. [CrossRef]
9. Zhu, D. Advanced environmental barrier coatings for SiC/SiC ceramic matrix composite turbine components, Engineered ceramics: Current status and future prospects. *M. Eng. Ceram. Curr. Status Future Prospect.* **2016**, 187–202. [CrossRef]
10. Harder, B.J. Oxidation performance of Si-HfO_2 environmental barrier coating bond coats deposited via plasma spray-physical vapor deposition. *Surf. Coat. Technol.* **2020**, *384*, 125311. [CrossRef]

11. Zhu, R.B.; Zou, J.P.; Mao, J.; Deng, Z.Q.; Zhang, X.F.; Deng, C.M.; Liu, M. A comparison between novel $Gd_2Zr_2O_7$ and $Gd_2Zr_2O_7$/YSZ thermal barrier coatings fabricated by plasma spray-physical vapor deposition. *Rare Met.* **2021**, *40*, 2244–2253. [CrossRef]
12. Zhu, D.; Miller, R.; Fox, D. Thermal and environmental barrier coating development for advanced propulsion engine systems. In Proceedings of the 48th AIAA/ASME/ASCE/AHS/ASC Structures, Structural Dynamics, and Materials Conference, Schaumburg, IL, USA, 7–10 April 2008; p. 2130.
13. Amer, M.; Curry, N.; Hayat, Q.; Sharma, R.; Janik, V.; Zhang, X.; Nottingham, J.; Bai, M. Cracking Behavior of $Gd_2Zr_2O_7$/YSZ Multi-Layered Thermal Barrier Coatings Deposited by Suspension Plasma Spray. *Coatings* **2023**, *13*, 107. [CrossRef]
14. Liu, S.; Liu, Q.; Hu, X.P.; Guo, J.W.; Zhu, W.; Zhang, F.; Xia, J. CMAS corrosion resistance behavior and mechanism of $Hf_6Ta_2O_{17}$ ceramic as potential material for thermal barrier coatings. *Coatings* **2023**, *13*, 404. [CrossRef]
15. Mehboob, G.; Liu, M.; Xu, T.; Hussain, S.; Mehboob, G.; Tahir, A. A review on failure mechanism of thermal barrier coatings and strategies to extend their lifetime. *Ceram. Int.* **2019**, *46*, 8497–8521. [CrossRef]
16. Yang, S.-J.; Song, W.-J.; Dingwell, D.B.; He, J.; Guo, H.-B. Surface roughness affects metastable non-wetting behavior of silicate melts on thermal barrier coatings. *Rare Met.* **2021**, *41*, 469–481. [CrossRef]
17. Guo, Y.Q.; Song, W.J.; Guo, L.; Li, X.X.; He, W.T.; Yan, X.D.; Dingwell, D.B.; Guo, H.B. Molten-volcanic-ash-phobic thermal barrier coating based on biomimetic structure. *Adv. Sci.* **2023**, *10*, 2205156. [CrossRef]
18. Guo, L.; Gao, Y.; Ye, F.X.; Zhang, X.M. CMAS corrosion behavior and protection method of thermal barrier coatings for aeroengine. *Acta. Metall. Sin.* **2021**, *57*, 1184–1198.
19. Mikulla, C.; Steinberg, L.; Niemeyer, P.; Schulz, U.; Naraparaju, R. Microstructure Refinement of EB-PVD Gadolinium Zirconate Thermal Barrier Coatings to Improve Their CMAS Resistance. *Coatings* **2023**, *13*, 905. [CrossRef]
20. Hu, X.; Liu, G.; Liu, Q.; Zhu, W.; Liu, S.; Ma, Z. Failure Mechanism of EB-PVD Thermal Barrier Coatings under the Synergistic Effect of Thermal Shock and CMAS Corrosion. *Coatings* **2022**, *12*, 1290. [CrossRef]
21. Poerschke, D.L.; Jackson, R.W.; Levi, C.G. Silicate Deposit Degradation of Engineered Coatings in Gas Turbines: Progress toward Models and Materials Solutions. *Annu. Rev. Mater. Res.* **2017**, *47*, 297–330. [CrossRef]
22. Poerschke, D.L.; Hass, D.D.; Eustis, S.; Seward, G.G.; Van Sluytman, J.S.; Levi, C.G. Stability and CMAS Resistance of Ytterbium-Silicate/Hafnate EBCs/TBC for SiC Composites. *J. Am. Ceram. Soc.* **2014**, *98*, 278–286. [CrossRef]
23. Godbole, E.; Von Der Handt, A.; Poerschke, D. Apatite and garnet stability in the Al–Ca–Mg–Si–(Gd/Y/Yb)–O systems and implications for T/EBC: CMAS reactions. *J. Am. Ceram. Soc.* **2021**, *105*, 1596–1609. [CrossRef]
24. Turcer, L.R.; Krause, A.R.; Garces, H.F.; Zhang, L.; Padture, N.P. Environmental-barrier coating ceramics for resistance against attack by molten calcia-magnesia-aluminosilicate (CMAS) glass: Part II, β-$Yb_2Si_2O_7$ and β-$Sc_2Si_2O_7$. *J. Eur. Ceram. Soc.* **2018**, *38*, 3914–3924. [CrossRef]
25. Liu, H.; Cai, J.; Zhu, J. CMAS (CaO-MgO-Al_2O_3-SiO_2) resistance of Y_2O_3-stabilized ZrO_2 thermal barrier coatings with Pt layers. *Ceram. Int.* **2018**, *44*, 452–458. [CrossRef]
26. Islam, A.; Sharma, A.; Singh, P.; Pandit, N.; Keshri, A.K. Plasma-sprayed CeO2 overlay on YSZ thermal barrier coating: Solution for resisting molten CMAS infiltration. *Ceram. Int.* **2022**, *48*, 14587–14595. [CrossRef]
27. Li, B.W.; Sun, J.Y.; Guo, L. CMAS corrosion behavior of Sc doped $Gd_2Zr_2O_7$ /YSZ thermal barrier coatings and their corrosion resistance mechanisms. *Corros. Sci.* **2021**, *193*, 109899. [CrossRef]
28. Chen, W.B.; He, W.T.; He, J.; Guo, Q.; Li, S.; Guo, H.B. Failure mechanisms of $(Gd_{0.9}Yb_{0.1})_2Zr_2O_7/Yb_2SiO_5$/Si thermal/environmental barrier coatings during thermal exposure at 1300 °C/1400 °C. *J. Eur. Ceram. Soc.* **2022**, *42*, 3297–3304. [CrossRef]
29. Yan, Z.; Guo, L.; Li, Z.; Yu, Y.; He, Q. Effects of laser glazing on CMAS corrosion behavior of Y2O3 stabilized ZrO2 thermal barrier coatings. *Corros. Sci.* **2019**, *157*, 450–461. [CrossRef]
30. Krämer, S.; Yang, J.; Levi, C.G.; Johnson, C.A. Thermochemical interaction of thermal barrier coatings with molten CaO-MgO-Al_2O_3-SiO_2 (CMAS) deposits. *J. Am. Ceram. Soc.* **2006**, *89*, 3167–3175. [CrossRef]
31. Guo, L.; Xin, H.; Li, Y.; Yu, Y.; Yan, Z.; Hu, C.; Ye, F. Self-crystallization characteristics of calcium-magnesium-alumina- silicate (CMAS) glass under simulated conditions for thermal barrier coating applications. *J. Eur. Ceram. Soc.* **2020**, *40*, 5683–5691. [CrossRef]
32. Gao, L.; Guo, H.; Gong, S.; Xu, H. Plasma-sprayed $La_2Ce_2O_7$ thermal barrier coatings against calcium–magnesium–alumina–silicate penetration. *J. Eur. Ceram. Soc.* **2014**, *34*, 2553–2561. [CrossRef]
33. Shing, O.P.; Ping, T.Y.; Hin, T.Y.Y. Mechanochemical synthesis and characterization of calcium-doped ceria oxide Ion conductor. *IOP Conf. Ser. Mater. Sci. Eng.* **2011**, *17*, 012017. [CrossRef]
34. Tsunekawa, S.; Sivamohan, R.; Ito, S.; Kasuya, A.; Fukuda, T. Structural study on monosize CeO2-x nano-particles. *Nanostructured Mater.* **1999**, *11*, 141–147. [CrossRef]
35. Yang, D.; Wang, L.; Sun, Y.Z.; Zhou, K.B. Synthesis of one-dimensional $Ce_{1-x}Y_xO_{2-x/2}$ (0 <= x <= 1) solid solutions and their catalytic properties: The role of oxygen vacancies. *J. Phys. Chem. C* **2010**, *114*, 8926–8932.
36. Yan, Z.; Guo, L.; Zhang, Z.; Wang, X.; Ye, F. Versatility of potential protective layer material Ti_2AlC on resisting CMAS corrosion to thermal barrier coatings. *Corros. Sci.* **2020**, *167*, 108532. [CrossRef]
37. Wolf, M.; Mack, D.E.; Guillon, O.; Vaßen, R. Resistance of pure and mixed rare earth silicates against calcium-magnesium-aluminosilicate (CMAS): A comparative study. *J. Am. Ceram. Soc.* **2020**, *103*, 7056–7071. [CrossRef]

38. Lyu, G.; Kim, I.-S.; Song, D.; Park, H.-M.; Kim, J.S.; Song, T.; Myoung, S.; Jung, Y.-G.; Zhang, J. Sintering behavior and phase transformation of YSZ-LZ composite coatings. *Ceram. Int.* **2019**, *46*, 1307–1313. [CrossRef]
39. Shi, Y.; Li, B.W.; Zhao, M.; Zhang, M.X. Growth of diopside crystals in CMAS glass-ceramics using Cr_2O_3 as a nucleating agent. *J. Am. Ceram. Soc.* **2018**, *101*, 3968–3978. [CrossRef]
40. Wiesner, V.L.; Bansal, N.P. Crystallization kinetics of calcium–magnesium aluminosilicate (CMAS) glass. *Surf. Coat. Technol.* **2014**, *259*, 608–615. [CrossRef]
41. Poerschke, D.L.; Levi, C.G. Effects of cation substitution and temperature on the interaction between thermal barrier oxides and molten CMAS. *J. Eur. Ceram. Soc.* **2015**, *35*, 681–691. [CrossRef]
42. Aygun, A.; Vasiliev, A.L.; Padture, N.P.; Ma, X. Novel thermal barrier coatings that are resistant to high-temperature attack by glassy deposits. *Acta Mater.* **2007**, *55*, 6734–6745. [CrossRef]
43. Guo, L.; Yan, Z.; Wang, X.; He, Q. Ti_2AlC MAX phase for resistance against CMAS attack to thermal barrier coatings. *Ceram. Int.* **2019**, *45*, 7627–7634. [CrossRef]
44. Hopkins, R.H.; De Klerk, J.; Piotrowski, P.; Walker, M.S.; Mathur, M.P. Thermal and elastic properties of silicate oxyapatite crystals. *J. Appl. Phys.* **1973**, *44*, 2456–2458. [CrossRef]
45. Krause, A.R.; Li, X.; Padture, N.P. Interaction between ceramic powder and molten calcia-magnesia-alumino-silicate (CMAS) glass, and its implication on CMAS-resistant thermal barrier coatings. *Scr. Mater.* **2016**, *112*, 118–122. [CrossRef]
46. Mechnich, P.; Braue, W.; Green, D.J. Volcanic ash-induced decomposition of EB-PVD $Gd_2Zr_2O_7$ thermal barrier coatings to Gd-oxyapatite, zircon, and Gd,Fe-Zirconolite. *J. Am. Ceram. Soc.* **2013**, *96*, 1958–1965. [CrossRef]
47. Guo, W.; Wang, Z.; Zhao, Z.; An, Z.; Wang, W. Effect of CeO_2 on the viscosity and structure of high-temperature melt of the CaO-SiO_2(-Al_2O_3)-CeO_2 system. *J. Non-Cryst. Solids.* **2020**, *540*, 120085. [CrossRef]
48. Turcer, L.R.; Padture, N.P. Rare-earth pyrosilicate solid-solution environmental-barrier coating ceramics for resistance against attack by molten calcia–magnesia–aluminosilicate (CMAS) glass. *J. Mater. Res.* **2020**, *35*, 2373–2384. [CrossRef]
49. Guo, L.; Li, G.; Wu, J.; Wang, X. Effects of pellet surface roughness and pre-oxidation temperature on CMAS corrosion behavior of Ti_2AlC. *J. Adv. Ceram.* **2022**, *11*, 945–960. [CrossRef]
50. Krause, A.R.; Senturk, B.S.; Garces, H.F.; Dwivedi, G.; Ortiz, A.L.; Sampath, S.; Padture, N.P. $2ZrO_2 \cdot Y_2O_3$ Thermal Barrier Coatings Resistant to Degradation by Molten CMAS: Part I, Optical Basicity Considerations and Processing. *J. Am. Ceram. Soc.* **2014**, *97*, 3943–3949. [CrossRef]
51. Chen, Q.; Qiao, Y.; Wang, H. Spectra and magneto optical behavior of CeO_2 doped heavy metal diamagnetic glass. *J. Non Cryst. Solids* **2017**, *470*, 70–77. [CrossRef]